Journal of Power Sources 181 (2008) 85–92

Contents lists available at ScienceDirect

Journal of Power Sources

journal homepage: www.elsevier.com/locate/jpowsour

Effective modulus and coefficient of thermal expansion of Ni–YSZ porous cermets

Janine Johnson, Jianmin Qu*

School of Mechanical Engineering, 801 Ferst Drive N.W., Georgia Institute of Technology, Atlanta, GA 30332-0405, United States

ARTICLE INFO

Article history:
Received 18 February 2008
Accepted 17 March 2008
Available online 22 March 2008

Keywords:
Stochastic
Fuel cell
Composite
Modulus
Thermal expansion
Finite element

ABSTRACT

Nickel zirconia, Ni–YSZ, porous cermets used in solid oxide fuel cells can be considered as composite materials consisting of three phases, namely nickel (Ni), ytrria-stabilized zirconia (YSZ), and voids. Based on Ni–YSZ's microstructural features, such as the volume fractions, average particle sizes and their correlations of a physical sample, a three-dimensional stochastic reconstruction method is used to recreate the three-phase composite. The digitally reconstructed microstructure is then transferred into finite element models to obtain the material's corresponding effective elastic modulus and effective coefficient of thermal expansion at various temperatures. Predictions from such a numerical methodology agree well with experimental results.

1. Introduction

Planar solid oxide fuel cells (SOFCs) are high-density power sources which promise relatively small environmental impact. Yet their widespread use is hindered by high costs and poor long-term thermomechanical reliability. Part of this reliability issue extends from thermal mismatch between the fuel cell layers and strict mechanical constraints from the SOFC configuration. For example, SOFCs are constructed of repeating layers of porous composites and solid ceramics across which the electrochemical reactions will take place. The composites are constructed of interpenetrating metals and ceramics, called cermets, that provide structural stability, efficient flow paths for fuel and air, and conduction pathways for ion transfer. Each of these functions is influenced by the respective arrangement and amount of metal and ceramic. Therefore there is a need to understand how the cermet's microstructure influences the thermomechanical properties of interpenetrating metal ceramic composites.

This work numerically creates multiple realizations (computer generated digital models of the material) of these composites to serve as a platform for numerical analyses. The realizations can then be used to determine material properties and their links to the microstructure.

The anode material, nickel-zirconia (Ni–YSZ), is a classic example of a three-phase porous material with a random heterogenous microstructure. Made by tape casting NiO-YSZ slurry, the final microstructure is highly influenced by starting particle sizes, constituent compositions, and the multi-step manufacturing process. The final microstructure is also influenced by the oxidation of NiO during the sintering process and fuel cell operation. Although Ni–YSZ's primary use is as a vehicle for ion transfer, the material must also meet several other requirements. It must provide structural support for the other layers in the cell; it must allow sufficient flow paths for fuels, and finally it must be able to handle temperature cycles from room temperature up to several hundred degrees Celsius. These requirements placed on the anode require a wide range of different material behaviors, and the enhancement of any of these can negatively impact another property.

In this paper Ni–YSZ is numerically generated as a three-phase composite made of overlapping spheres of nickel and YSZ with a porous matrix. The digital reconstruction method recreated a three-dimensional pixilated image, or realization, of the material. Since the reconstruction is 3D, the term voxel will be used in place of pixel. By generating multiple realizations, the statistical variation of key material properties, such as modulus and the coefficient of thermal expansion (CTE), can be determined.

Reconstruction and analysis of heterogenous structures takes place down several avenues. Fiber and particulate composites can be reconstructed through tessellation procedures and then analyzed using self-consistent methods. Pyrz studied fiber composites

* Corresponding author. Tel.: +1 404 894 5687; fax: +1 404 894 0186.
E-mail address: jianmin.qu@me.gatech.edu (J. Qu).

0378-7753/$ – see front matter © 2008 Elsevier B.V. All rights reserved.
doi:10.1016/j.jpowsour.2008.03.035

using Dirichelet tessellations for simulated hard core models and microscopy images, respectively [1]. Further research by Bochenek and Pyrz studied unidirectional fiber reinforced composites and particulate composites with Voronoi tessellations [2]. Stress interactions around the particles were calculated using superposition and the effective medium approach.

Ghosh and co-workers have directly incorporated representative volume elements (RVEs) generated from Voronoi cell (VC) tessellations into a multi-scale finite element method (FEM) [3–6]. The microstructural model is termed VC-FEM, and it models particulates in a matrix using Voronoi tessellations, where each tessellation is treated as an element with a particle at its center [3]. The same method was used for a multi-scale damage analysis in porous materials [5]. Additionally, three-dimensional models were created through stereological methods for particle reinforced metal matrix composites [4]. Next the concept of statistically equivalent representative volume elements (SERVEs) was used with VC-FEM to study fiber and particulate composites that varied randomly within the microstructure [7,8]. Methods developed by Gokhale and co-workers used extremely detailed images of the particulates in heterogenous microstructures to recreate the material through a controlled re-distribution methodology [9–12]. Another work examined the most efficient RVE size for use in macro–micro analysis for fiber composites [13]. Other methods perform finite element analyses on the actual microstructures read in via open source software OOF; then the FE model can be used for different studies, such as Cannillo's and Carter's stochastic damage analysis on a polycrystalline microstructure [14].

A modification of the simulated annealing method is used here for its flexibility and efficiency in creating multiple realizations for numerical analysis. Rintoul and Torquato used the simulated annealing method to reconstruct a distribution of spheres using the radial distribution function [15]. Next the simulated annealing method was used to recreate digitized media by Yeong and Torquato [16]. Yeong and Torquato minimized processing time by calculating the 2-point correlation function and the lineal chord function in orthogonal directions and then updating the functions only along rows and columns with one to one pixel exchanges. Manwart and Hilfer noted that the time saving device of calculating correlation functions in only orthogonal directions will only introduce anisotropy effects for microstructures displaying significant short-range order [17]. The impact of short-range order and the behavior of the simulated annealing procedure is further analyzed by Cule and Torquato [18]. Microstructural information from a 2D slice can also be used to construct a three-dimensional image as shown in Part II of Yeong's and Torquato's work on reconstructing random media [19]. Rozman and Utz used several techniques to improve the efficiency of the Monte Carlo reconstruction; these include using the Great Deluge Algorithm plus an additional criterion for "uphill" moves, limiting pixel changes to the interface, and calculating perturbations of the probability functions [20].

The material properties for random media can be determined through analytical, numerical, or experimental means. However, each method has limitations. For random co-continuous media analytical approaches are limited by microstructural information, and this is especially true for porous media. Unit cell models will be limited to very simple composites. Variational methods to determine bounds, such as Hashin–Sthrikman, will diverge away from the upper bound due to porosity. Experimental methods, while vital, are also severely limited by expense and efficiency. While software such as OOF can input one image of a material, it becomes significantly more difficult to study the variation of relevant material properties. Additionally, two-dimensional reconstruction techniques such as tessellations can accurately capture the behavior of a material, but cannot be easily adapted to the behavior of a three-dimensional random interpenetrating composite. To that end numerical reconstruction methods in connection with finite element analysis can become a fast and flexible way to determine realistic material properties with specific microstructures.

The simulated annealing method will be used to create voxel reconstructions for numerical analysis. The effective modulus and coefficient of thermal expansion will be found using multiple FE analyses. These analyses will also investigate size effects of the voxel reconstruction and the statistical variation of the results.

The following work will be arranged as follows. First, Section 2 will introduce the methodology behind random media and probability functions. Section 2.3 will specifically cover the reconstruction method used, and Section 2.4 will introduce the FE model. Section 3 will go over the results of the reconstruction, model convergence, and the effective properties. The last two sections will discuss these results in detail.

2. Methodology

2.1. Random media

For any media of volume V_i the microstructure can be fully characterized by an indicator function

$$I^{(i)}(\tilde{x}) = \begin{cases} 1, & \text{if } \tilde{x} \in V_i \\ 0, & \text{otherwise} \end{cases}, \tag{2.1}$$

where i is the phase number, and $\tilde{x}$ is the vector location within the volume [21]. The microstructure is assumed to be static and therefore is not a function of time.

The indicator function describes every possible point with a material, such that for any number, k, of phases the following equality holds,

$$\sum_{i=1}^{k} I^{(i)}(\tilde{x}) = 1. \tag{2.2}$$

With the indicator function random media can be described by determining the probability of a desired event or occurrence. For example, an event of interest could be when multiple points lie within the same phase. Such an event is an example of the n-point probability function as illustrated in (2.3).

$$S_n^{(i)}(\tilde{x}_1, \tilde{x}_2, \ldots, \tilde{x}_n) = P(I^{(i)}(\tilde{x}_1) = 1, I^{(i)}(\tilde{x}_2) = 1, \ldots, I^{(i)}(\tilde{x}_n) = 1), \tag{2.3}$$

where P indicates the probability that a given location lies within phase i. As the order n increases more microstructural details are captured.

If the probability distributions of a material are invariant with respect to location, the material is statistically homogenous and the material is called ergodic. Additionally, if the random media does not depend on the orientation of the vector positions, but only on the magnitude of the distance between the points, it can be considered isotropic. In this case, the n-point functions now become functions of the distance between the points such that $r = |\tilde{x}_j - \tilde{x}_i|$.

Thus for homogenous media the 1-point function will reduce to the volume fraction (φ_i) of the material,

$$S_1^{(i)} = P(I^{(i)}(\tilde{x}_j)) = \varphi_i, \tag{2.4}$$

and the 2-point functions become functions of distance r,

$$S_2^{(i)}(r) = S_2^{(i)}(\tilde{x}_1, \tilde{x}_2) = P(I^{(i)}(\tilde{x}_1) = 1, I^{(i)}(\tilde{x}_2) = 1). \tag{2.5}$$

Bounds exist for the 2-point function in homogenous media as the radius reduces to zero or extends to infinity. These are

$$\lim_{r\to 0} S_2^{(i)}(r) = \varphi_i \tag{2.6}$$

and

$$\lim_{r\to \infty} S_2^{(i)}(r) = (\varphi_i)^2. \tag{2.7}$$

In Eq. (2.6) the 2-point functions reduce to the 1-point function as r decreases and the two points converge to each other. In Eq. (2.7), as the distances between the points increase they are no longer spatially correlated and the 2-point approach becomes equivalent to calculating the 1-point function at two separate points.

The behavior of the 2-point probability function as r approaches zero is the first hint of the relationship between the probability functions for multiple phases. Torquato and Stell showed that any n-point probability function can be written as a function of the other phases [22]. In other words, for a two-phase material the description of one phase will guarantee its complement to the second phase. However, as the number of phases increases the relationship must also be quantified between the phases, i.e. for three phases there are actually multiple phases, namely phase 1, phase 2, phase 3, and the combinations of any two phases.

2.2. Microstructure

For this work the nickel and zirconia phases are described as overlapping spheres as defined by Weissberg [21,23]. The 2-point probability function does not exhibit any short-range order and is defined by one characteristic length, the particle diameter (d). At this point the function has reached its long-range order shown in (2.7). While the function controls particle size it does not correlate the particles together, which allows interpenetration to occur, and the most significant factor on clustering will be the volume fraction. The analytical expression for overlapping spheres uses the Heaviside function (Θ) as shown in (2.8).

$$S_2^{(i)} = 1 - 2(1-\varphi_i) + (1-\varphi_i)^{(4g(r)/\pi d^2)},$$

$$\text{where } g(r) = \frac{d^2}{2}\left(\pi - \Theta(d-r)(\arccos(r/d) - (r/d)\sqrt{1-r/d})\right) \tag{2.8}$$

A third function is now required to create each realization. For the three phases, the porous phase was the matrix of the composite; however, since no analytical function exists for this value it was approximated from one run of the material. The estimated 2-point function for the pore phases will satisfy the bounds in (2.6) and (2.7), but can exhibit short-range order.

2.3. Reconstruction

The realizations were generated using the digitized simulated method introduced by Lee and Torquato with modifications from Rozman and Utz [3,20]. The algorithms were implemented in the C++ language and the GNU GCC compiler [24]. The reconstruction procedure modifies the indicator function in Eq. (2.2) until the sample matches the desired probability functions. Then the indicator function is used to create a voxel representation of the material for further numerical use. Each voxel represents a different phase. The multiple step process is described below:

1. Randomly seed sample with volume fractions of each materials.
2. Calculate desired probability functions in the current realization.

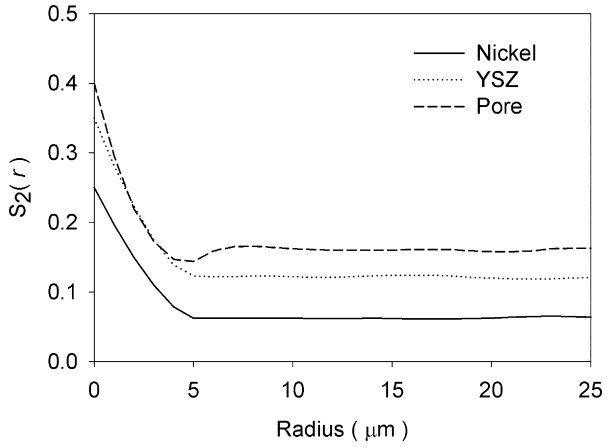

Fig. 1. 2-Point probability functions for reconstructed Ni–YSZ where nickel and YSZ are overlapping spheres with a 5 μm diameter.

3. Exchange random voxels. The exchanging of voxels was constrained such that the volume fraction of all three phases was maintained.
4. Update probability functions of volume and calculate energy.
5. Accept or reject change.
6. Repeat until an accepted criterion is reached.

The efficiency of the process was increased by using voxel selection at the interface, by sampling in orthogonal directions, by using the great deluge algorithm, and by using perturbations to calculate the correlation functions. Boundaries are periodic.

Part of the flexibility of the DIB reconstruction is the flexibility inherent in the use of energy as an acceptance criterion [16]. Any desired correlation function can be used and these individual functions can be weighted as desired. The energy function minimizes the least square difference between a given set of desired probability functions and the functions existing at the current time step of the reconstruction. Use of the least squares difference allows flexibility in the reconstruction by allowing different probability functions to be used at different weights.

2.4. FE model

The commercial software ABAQUS was used to perform the finite element analysis. For each digital image reconstructed, the voxels were transferred to eight node brick elements and input into a FE

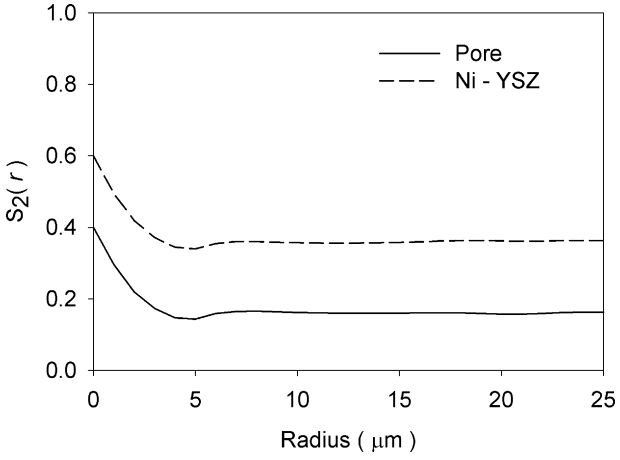

Fig. 2. 2-Point probability functions for the porous phase and the Ni–YSZ phase.

Table 1
Constituent material properties used in FE analysis at 25 °C

Material	Modulus (GPa)	Poisson's ratio	Referance
Nickel	207	.31	[27]
YSZ	216	.315	[28]

model. Perfect bonding was assumed between the elements, and each element was assigned the material properties corresponding to the digital reconstruction. The Young's modulus and coefficient of thermal expansion of the volume were calculated in each coordinate direction. The Young's modulus was calculated at room temperature using a standard structural analysis, while the CTE was calculated for a temperature range between 20° and 1000°.

The constituent material properties were temperature dependant and were taken from the literature referenced in Table 1. Experimental studies of the electrolyte material, non-porous 8 mol% ytrria (YSZ) material, were used as the YSZ properties in the Ni–YSZ composite. The behavior of nickel around the Curie point is complicated by the sudden jump in thermal expansion from the ferromagnetic transition; therefore a temperature dependent equation of CTE was used from the work of Faisst [25]. This expression was used to provide the CTE from 0 to 1000 °C. The CTE values for nickel and YSZ are included in Fig. 9.

3. Results

3.1. Realization reconstruction

Ni–YSZ is usually made from a precursor of NiO-YSZ, and a commonly used composition in fuel cells is 75% NiO/25 mol% YSZ [26]. When the anode material is fully reduced to Ni–YSZ, studies have found the volume porosity to be 40% and the nickel and YSZ ratios can be calculated to be 25% and 35%, respectively [26]. For both nickel and YSZ, the sphere diameter was set to 5 μm and the initial total length of the sample was 50 μm. One realization was generated with nickel and YSZ modeled as overlapping spheres. The pore probability function from this realization was smoothed for long-range order and then used for all further realizations. Fig. 1 shows the 2-point probability function for all three phases for a realization generated from all three probability functions. The pore function shows short-range order that vanishes before 8 μm. Fig. 2 compares the 2-point probability function of porosity to the combined nickel and zirconia phases. It can be seen that the length and magnitude of the short-range order are comparable. The 2-point pore function plotted in Fig. 1 is used for all future realizations and now each phase is governed by a probability function.

An additional probability function was calculated from the finished realization. The lineal chord function measures the probability that a chord connecting two random points in a phase *i* will lie in the same phase *i*. The lineal chord functions for each phase are plotted in Fig. 3. Examination of the plot shows that no significant chord lengths exist past 15 μm, approximately three times the particle diameters of nickel and YSZ.

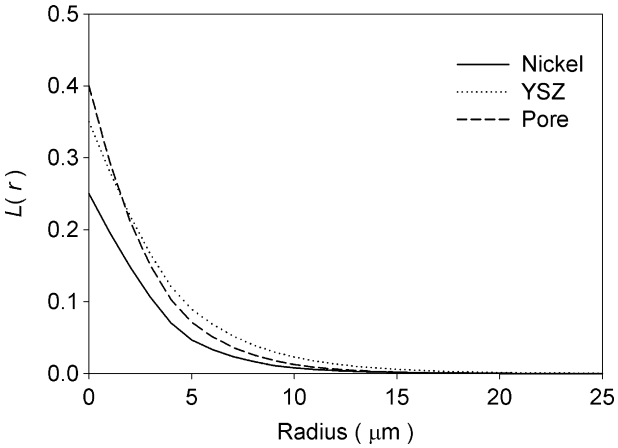

Fig. 3. Lineal chord functions for each phase in the realization.

3.2. Model convergence

After converting the realization to the FE model, convergence was tested by two different methods: discretization error and representative volume element size. Mesh density was tested by subdividing each voxel into four subsections and rerunning the analysis, and no significant difference was found to occur. Examination of discretization error determines that the voxel size is small enough to accurately capture material behavior, while the RVE size ensures that a large enough sample of the material is analyzed to capture the material behavior. Separate tests were performed for both the modulus and the CTE, since RVE size and discretization error could vary depending on the analysis type.

3.2.1. Discretization

Table 2 presents the calculated modulus for five different realizations in three directions providing a sample size of 15. The length is maintained at 50 μm while the total number of voxels used to measure the sample is increased. The size of the model is measured in the number of divisions along each side of the cube. The physical dimensions of the particle diameters and the porosity's characteristic length are also constant for each size. The mean (χ) is listed and the standard deviation (S) is also recorded. The same procedure is repeated in Table 3 for the CTE. The models selected as converged are shaded in light grey.

3.2.2. RVE size

Testing of the RVE size means that the dimensions of the sample size will change while the physical size of each voxel stays constant. Table 4 shows the modulus results, and the RVE size is varied from

Table 2
Discretization of modulus at 25 °C

Model #	Number	Division	Length (μm)	d (μm)	χ (GPa)	S	% Difference
1	15	10	50	1	84.97	8.60	-
2	15	20	50	2	78.33	4.39	7.82
3	15	30	50	3	73.78	5.10	5.81
4	15	40	50	4	71.25	3.91	3.43
5	**15**	**50**	**50**	**5**	**69.29**	**3.26**	**2.76**
6	15	60	50	6	69.51	3.96	0.32

Table 3
Discretization of CTE at 1000 °C

Model #	Number	Division	Length (μm)	d (μm)	χ (°C^{-1} x 10^{-6})	S	% Difference
1	15	10	50	1	14.04	0.26	
2	15	20	50	2	14.20	0.14	1.13
3	**15**	**30**	**50**	**3**	**14.19**	**0.09**	**0.09**

Table 4
RVE Size of modulus at 25 °C

Model #	Number	Division	Length (μm)	d (μm)	χ (GPa)	S	% Difference
7	15	10	10	5	-	-	-
8	15	20	20	5	37.25	9.12	-
9	15	30	30	5	70.16	5.83	88.34
10	15	40	40	5	70.09	4.33	0.09
11	**15**	**50**	**50**	**5**	**69.29**	**3.26**	**1.15**
12	15	60	60	5	70.66	2.45	1.98

Table 5
RVE Size of CTE at 1000 °C

Model #	Number	Division	Length (μm)	d (μm)	χ (°C^{-1} x 10^{-6})	S	%Difference
13	15	10	16.7	5	-	-	-
14	15	20	33.3	5	14.10	0.24	-
15	**15**	**30**	**50.0**	**5**	**14.19**	**0.09**	**0.63**
11	9	40	66.7	5	14.23	0.05	0.27

the result of 50 divisions from Table 2. Table 5 repeats the procedure for CTE.

3.2.3. Final realizations

Box plots of the mean and standard deviation of the modulus illustrate the differences between the two different kinds of convergence. In Fig. 4a the mean of the modulus decreases significantly as the voxel length is decreased, until both the mean and standard deviation do not vary significantly. However, in Fig. 4b the mean varies little after the first sample, while the standard deviation continues to vary.

The measurements of CTE showed slightly different behavior by being far less dependent on voxel size, but slightly more dependent on RVE size. Yet, since thermal expansion is primarily a constraint issue, far fewer elements are needed for accurate calculation of CTE coefficients.

The final models used for further analysis are shown in Fig. 5a and b. A quarter section of the model is removed to show the microstructure within the 3D reconstruction.

3.3. Computational expense

The ability to select the minimum model needed for analysis is significant due to the computational expense. Since the reconstructions are three-dimensional a slight increase will eventually lead to significant increases in the time to reconstruct Ni–YSZ. This is born out in Fig. 6 which plots the clock time per second versus the model divisions. However, it should be noted that computational expense is strictly a matter of total elements and complexity of the reference functions used.

3.4. Material properties

3.4.1. Modulus

Based on the discussion above, models with 50 divisions were selected for computing the elastic modulus. Fifty different realiza-

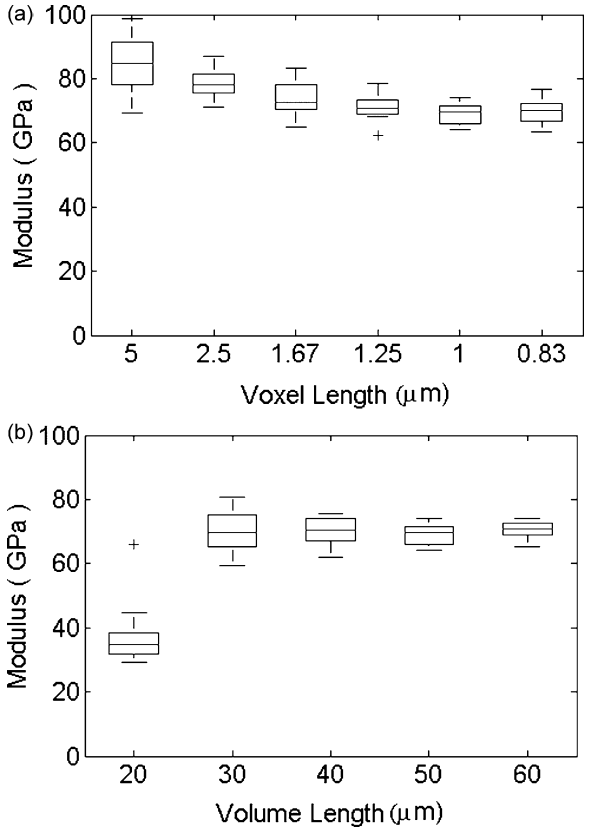

Fig. 4. Box plots of modulus for (a) discretization error and (b) RVE size at 25 °C.

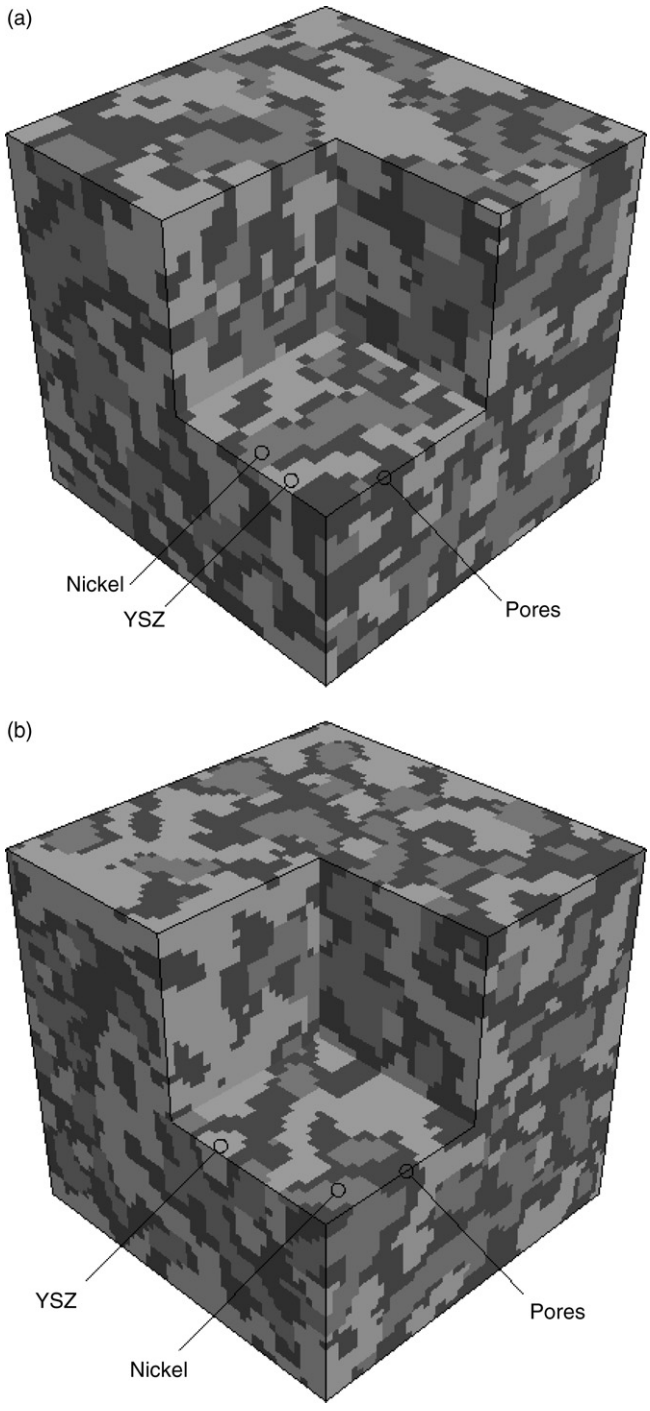

Fig. 5eps. Final realizations of Ni–YSZ for the (a) CTE model with 30 divisions and (b) Young's modulus model with 50 divisions.

tions were constructed and analyzed in each coordinate direction to obtain the effective elastic modulus. The results are best fit to a normal distribution, even though there is a right leaning skew as shown in Fig. 7.

3.4.2. Coefficient of thermal expansion

Since the CTE had very small standard deviations, the FE analysis focused on the CTE variation due to change in temperature. Fig. 8a shows the nickel, Ni–YSZ, and YSZ CTEs for 0–1000 °C. The CTE is linear except at the Curie point of nickel at 349 °C. The Curie point behavior is zoomed in on in Fig. 8b.

4. Discussion

4.1. Realization reconstruction

The simulated annealing method efficiently recreated many different realizations of the given Ni–YSZ microstructure. The 2-point probability function also proved sufficient in recreating the microstructure so long as each of the three phases was described. In Fig. 1 the plots of the nickel and YSZ match almost exactly the analytical functions of overlapping spheres. Additionally, for all realizations listed in Tables 2–5 the final reconstructions had probability functions identical to the reference functions.

The importance of using the pore probability function is clear in Fig. 2. The function matches the bounds in Eqs. (2.6) and (2.7), which means the pore phase behaves in a random manner. The short-range order in the pore phase is also a good fit with the short-range order in the combined nickel and YSZ phases. This is reasonable; since the initial realization was created using only the two overlapping sphere functions, the remaining pore phase would have been forced in a controlled distribution around the spheres.

The lineal chord plot in Fig. 3 provides limited information on the clustering behavior of the microstructure. The majority of chord lengths are limited to the diameter size for all three phases. The YSZ phases show slightly more clustering than the nickel phase, which is reasonable since YSZ has a higher volume fraction. The fact that the pore phase, which has the highest volume fraction in the material, shows less clustering would be a cause of the short-range order in its 2-point probability function.

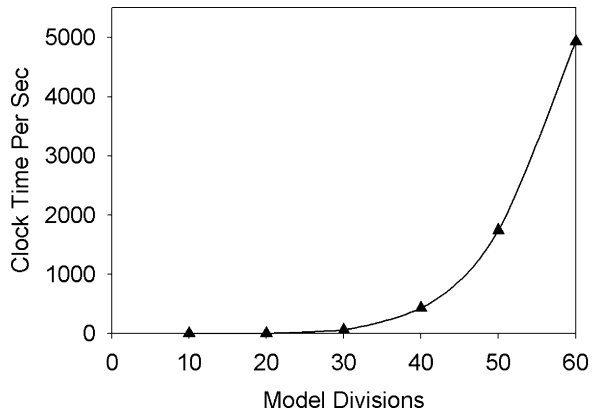

Fig. 6. Clock time per second versus the model divisions during reconstruction.

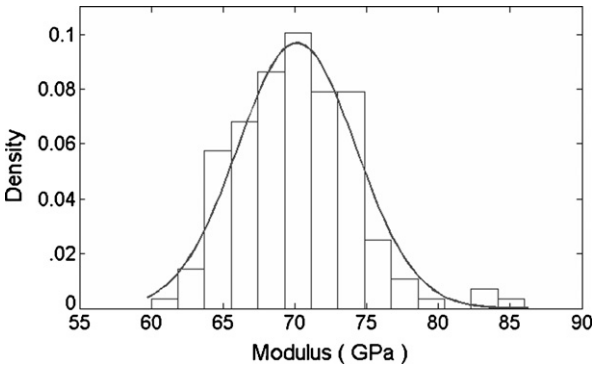

Fig. 7. Statistical variation of Young's modulus for 50 total realizations measured in three directions with a model size of 50 divisions at 25 °C, a particle diameter of 5 μm, and a volume length of 50 μm.

4.2. Model convergence

The two different convergence tests had different results depending on the material property measured. While the Young's modulus was dependent on both voxel size and the total volume size, the CTE was insensitive to changes in either. By comparing the discretization and RVE results plotted in Fig. 4, different conclusions can be drawn about the FE determination of the Young's modulus. First, as voxel size decreases the modulus will be more accurately captured, as the voxels more accurately capture the microstructures' behavior. Secondly, once a sufficient RVE is found, a continued increase of volume will affect the standard deviation of the modulus while the mean stays constant. This makes sense; as the volume grows it behaves in an increasingly homogenous manner. Thermal expansion, as a constraint problem, was very insensitive to discretization error and was much more dependant on RVE size.

4.3. Material properties

Compared to the Hashin–Shtrikman upper bounds for the Young's modulus, these results are very reasonable as shown in Fig. 9 [27]. Work by Radovic et al. has predicted the modulus results for 40% porosity to be approximately 60 GPa, which is 22% lower than our calculated value [26]. However, since the realization microstructure is generated using an exact description of overlapping spheres, it is safe to assume the microstructures are significantly different.

The slight right leaning skew of the modulus results (Fig. 7) suggests that the modulus tends upward. The exact reason for this is unknown, but could be because a lower limit of the modulus is more a function of volume fractions than microstructural arrangement. Our lower bound of 60 GPa does compare with experimental results.

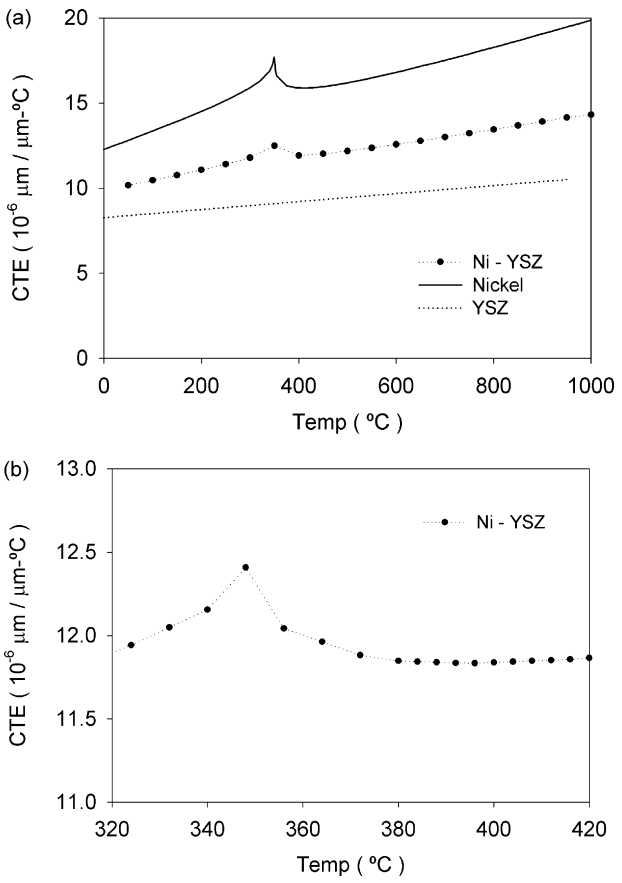

Fig. 8. CTE of Ni–YSZ with respect to temperature for (a) 0–1000 °C and (b) around the Curie point.

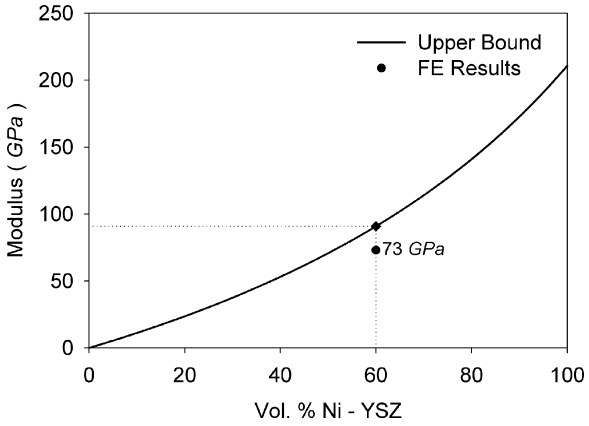

Fig. 9. Hashin–Shtrikman upper bound of modulus with respect to vol.% Ni–YSZ.

The FE results for CTE match closely experimental results, which range from 10.5e-6 to 14e-6 for 100–950 °C [28]. It is interesting that CTE measure had such small standard deviations for every model configuration analyzed. From Tables 3 and 5 it appears that CTE is primarily a function of volume fraction. Also the CTE requires a sufficient RVE size to be accurately measured. The plots of CTE for Ni–YSZ (Fig. 8) show that the CTE is almost equally divided between the constituent materials, and that it also has linear behavior except at the Curie point.

5. Conclusions

The two point correlation functions for overlapping spheres were used to digitally recreate the material nickel zirconia used for SOFC anodes. Next finite element analyses were used to determine the Young's modulus and CTE of Ni–YSZ. The FE models accurately captured the microstructural variation within the composite. Study of multiple realizations showed that different microstructures with the same statistical features behave in a relatively uniform manner after convergence is reached. To that end, the reconstruction method can be used to create models for FE analysis to study the stochastic nature of metal–ceramic composites.

Although only elastic modulus and CTE are considered in this paper, the reconstruction method developed here can also be used to study other mechanical and thermal behaviors of multi-phase composites, such as fracture, fatigue, creep, and effective thermal conductivity, as well as flow properties such as permeability. Results of these studies will be published elsewhere.

Acknowledgements

With thanks to Oak Ridge National Laboratory for material samples and properties. The research was supported partially by NSF (CMMI 0726286).

References

[1] R. Pyrz, Composites Sci. Technol. 50 (2) (1994) 197.
[2] B. Bochenek, R. Pyrz, Comput. Mater. Sci. 31 (1–2) (2004) 93.
[3] K. Lee, S. Moorthy, S. Ghosh, Comput. Methods Appl. Mech. Eng. 172 (1–4) (1999) 175.
[4] M. Li, et al., Mater. Sci. Eng. A (Struct. Mater.: Properties, Microstruct. Process.) A266 (1–2) (1999) 221.

[5] S. Ghosh, K. Lee, P. Raghavan, Int. J. Solids Struct. 38 (14) (2001) 2335.
[6] P. Raghavan, S. Li, S. Ghosh, Finite Elements Anal. Des. 40 (12) (2004) 1619.
[7] P. Raghavan, S. Ghosh, Comput. Model. Eng. Sci. 5 (2) (2004) 151.
[8] S. Swaminathan, S. Ghosh, N.J. Pagano, J. Composite Mater. 40 (7) (2006) 583.
[9] Z. Shan, A.M. Gokhale, Int. J. Plast. 20 (2004) 1347–1370.
[10] Y. Mao, A.M. Gokhale, J. Harris, Comput. Mater. Sci. 37 (4) (2006) 543.
[11] H. Singh, et al., Acta Mater. 54 (8) (2006) 2131.
[12] H. Singh, et al., Model. Simulation Mater. Sci. Eng. 3 (2006) 351.
[13] Z. Shan, A.M. Gokhale, Comput. Mater. Sci. 24 (3) (2002) 361.
[14] V. Cannillo, W. Craig Carter, J. Mater. Sci. 40 (15) (2005) 3993.
[15] M.D. Rintoul, S. Torquato, J. Colloid Interface Sci. 186 (2) (1997) 467–476.
[16] C.L.Y. Yeong, S. Torquato, Phys. Rev. E (Stat. Phys., Plasmas, Fluids, Related Interdisciplinary Topics) 57 (1) (1998) 495.
[17] C. Manwart, R. Hilfer, Phys. Rev. E (Stat. Phys., Plasmas, Fluids, Related Interdisciplinary Topics) 59 (5) (1999) 5596.
[18] D. Cule, S. Torquato, J. Appl. Phys. 86 (6) (1999) 3428.
[19] C.L.Y. Yeong, S. Torquato, Phys. Rev. E (Statistical Phys., Plasmas, Fluids, Related Interdisciplinary Topics) 58 (1) (1998) 224.
[20] M.G. Rozman, M. Utz, Phys. Rev. E 63 (2001) 8.
[21] S. Torquato, Random Heterogeneous Materials: Microstructure and Macroscopic Properties, Interdisciplinary Applied Mathematics, vol. 16, Springer, New York, 2002, p. 699.
[22] S. Torquato, G. Stell, J. Chem. Phys. 77 (4) (1982) 2071.
[23] H.L. Weissberg, J. Appl. Phys. 34 (9) (1963) 2636.
[24] GCC, the GNU Compiler Collection. Accessed Available from: http://gcc.gnu.org/.
[25] T.A. Faisst, J. Phys.: Condensed Matter 1 (33) (1989) 5805.
[26] M. Radovic, E. Lara-Curzio, et al., Effect of hydrogen reduction on the microstructure and elastic properties of Ni-based anodes for SOFCs, Ceramic Transactions, v 161, Developments in Solid Oxide Fuel Cells and Lithium Ion Batteries – Proceedings of the 106th Annual Meeting of the Ceramic Society, 2005, pp 41–50.
[27] Z. Hashin, S. Shtrikman, J. Mech. Phys. Solids 11 (127–140) (1963).
[28] M. Radovic, et al., Thermophysical properties of YSZ and Ni-YSZ as a function of temperature and porosity, Advances in Solid Oxide Fuel Cells II, A Collection of Papers Presented at the 30th International Conference on Advanced Ceramics and Composites, 2006, pp 79–85.